Experimental and numerical investigations on hydro-mechanical properties of saturated fine-grained sandstone

Susheng Wang, Weiya Xu, Wei Wang

Version of Record: https://www.sciencedirect.com/science/article/pii/S1365160918311079
Manuscript_a6b825737a121acc9c6640d5bbf01596

IJRMMS-2018-1025 – edited and approved by editor

Experimental and numerical investigations on hydro-mechanical properties of saturated fine-grained sandstone

Technical Note

Susheng Wang[a,b,c,*], Weiya Xu[a,b], Wei Wang[a,b]

a. Key Laboratory of Ministry of Education for Geomechanics and Embankment Engineering, Hohai University, Nanjing, Jiangsu 210098, China

b. Institute of Geotechnical Engineering, Hohai University, Nanjing, Jiangsu 210098, China

c. Laboratory of Multiscale and Multiphysics Mechanics, University of Lille, CNRS FRE 2016, LaMcube, Lille, 59000, France

Abstract: In order to investigate hydro-mechanical properties of fine-grained sandstone in Xiangjiaba hydropower station in China, a series of triaxial compression tests of saturated fine-grained sandstone were conducted. Two groups of hydro-mechanical triaxial compression tests of saturated sandstone are conducted: firstly, confining pressure is constant at 10 MPa while pore pressure is varied from 4, 6, and 8 MPa; secondly, pore pressure is constant at 6 MPa while confining pressure is varied from 10, 15, and 20 MPa. The effects of the confining and pore pressures on strength and deformation behaviors of saturated fine-grained sandstone are discussed. Based on the test results, a novel coupled elastoplastic damage model is proposed to considering hydro-mechanical coupling properties of saturated fine-grained sandstone using the effective stress concept. Furthermore, the numerical formulations of a return mapping algorithm for the coupled model implementation are introduced in detail. Finally, the validity and efficiency of the model are compared between numerical simulation and test results. Therefore, the coupled model is effectively applied in the stability analysis of practical engineering.

Keywords: Fine-grained sandstone; Triaxial compression test; Hydro-mechanical properties; Coupled elastoplastic damage model

1. Introduction

Brittle rock, such as granite gneiss [1], shale [2], limestone [3], and sandstone [4] et al. as building materials are widely used in water conservancy project. The mechanical behaviors of brittle rock are complex, including pre-peak strain hardening and the post-peak softening, confining pressure dependent, volumetric dilatancy, stiffness degradation, irreversible deformation, etc. Fine-grained sandstone is widely used in Xiangjiaba hydropower station, in China. The strength of fine-grained sandstone on the condition of seepage is related to the success of reservoir impoundment. In order to provide bases for the engineering design and safe evaluation, experimental and numerical investigation on mechanical behaviors of saturated fine-grained sandstone should be performed.

Extensive experimental studies on brittle rocks have been conducted, including stress path, structural anisotropy, time-dependent effect, mineral composition, hydro-mechanical behavior et al. Two nonlinear deformation mechanisms of fine-grained sandstone are generally identified, accumulation irreversible deformation and stiffness degradation [5]. Many investigation results indicate that pore pressure has an indisputable effect on mechanical behaviors and deterioration of strength and stiffness properties of rock material [6-8]. Besides, the experimental results also indicate that the strength of rock increases with the decreasing of grain size [9-11]. Previous works are focused on the mechanical properties of sandstone with relatively coarse grains and higher porosity. The strength and deformation behaviors of dry fine-grained sandstone have been studied by experimental and modeling methods [4]. However, the impact of pore pressure on deformation and failure mechanism of fine-grained sandstone has not been studied so far. Therefore, the key work of this work is further to study the hydro-mechanical behaviors of saturated fine-grained sandstone.

Two approaches to develop constitutive models for rock materials by considering the irreversible deformation and damage evolution: micromechanical and phenomenological methods. From a microscopic point of view, microcrack growth and frictional sliding along closed cracks accounting for physical mechanisms are the issues for governing the inelastic mechanical behaviors of quasi-brittle materials [12-14]. Due to the difficult methods of describing microcracks growth and the complex formulation and identification parameters of micromechanical model, few of such models have been applied to the practical engineering. From a phenomenological point of view, two internal variables are defined to describe the degradation of material and plastic deformation in constitutive model. As it is easily for finite element method implementation, coupled phenomenological constitutive equations are

used in underground powerhouse and tunnel project [3, 15]. For the phenomenological seepage constitutive model, the first approach is account for using effective stress principle for saturated geomaterial [16-21], the second one is formulated in the thermodynamic framework of partially saturated media [22-24]. Both of them reveal the mechanical behaviors of geomaterial seepage flow. However, the former is more suitable for saturated porous materials while the latter is questionable to concern with capillary pressure in a porous saturated rock test. The effective stress concept is validated by studying the strength and deformation behaviors of porous rock materials in both drained triaxial compression tests [21, 25, 26]. Therefore, we couple irreversible deformation, damage evaluation, and hydro-mechanical properties into the constitutive modelling using effective stress principle to obtain realistic and consistent results.

In this study, a series of hydro-mechanical coupling triaxial compression tests are conducted to reveal the hydro-mechanical properties of fine-grained sandstone. Compared the experimental results of dry and saturated fine-grained sandstone, the effects of confining and pore pressures on mechanical behaviors of the sandstone are discussed. Based on experimental results, a new coupled elastoplastic damage model is proposed to describe hydro-mechanical coupling properties of saturated fine-grained sandstone. Meanwhile, an exponential form of damage criterion is defined to describe the damage evolution. The numerical formulation of the proposed model implemented is introduced in details. The method of identification of model's parameters is also given. Finally, the reliability and veracity of the coupled model is validated by comparing with the experimental results of fine-grained sandstone.

2. Experimental investigations

2.1 Rock specimens

The studied rock samples are typical fine-grained sandstone from the right bank of Xiangjiaba Hydropower Station in China. The saturated density of fine-grained sandstone is 2.63 g/cm^3 and the mean porosity is 2.64%. According to the method suggested of the International Society of Rock Mechanics, all tested fine-grained sandstone samples are prepared as cylinders with a length of 100 mm and 50 mm in diameter. The typical dry and saturated fine-grained sandstone samples are shown in Fig. 1.

2.2 Experimental method

A servo-controlled triaxial rock rheology test system, which is developed by Hohai University in China, is used for triaxial compression test of dry and saturated fine-grained sandstone. Triaxial compression tests of dry fine-grained sandstone under confining pressures 0, 3, 5, 10, 15, and 20 MPa were conducted. More detailed description of the test procedures are introduced in [4].

In order to consider the influence factors of confining and pore pressures on saturated fine-grained sandstone, two groups of hydro-mechanical triaxial compression tests are conducted: firstly, confining pressure is constant at 10 MPa while pore pressure is varied from 4, 6, and 8 MPa; secondly, pore pressure is constant at 6 MPa while confining pressure is varied from 10, 15, and 20 MPa. All fine-grained sandstone samples were fully saturated with water in a vacuum of negative pressure (-0.098 MPa) for 24h before the test. All tests are performed in drained condition. The experimental procedures from are as follows:

(1): The samples are placed in triaxial cell. Then make pressure chamber filled with oil.

(2): The hydrostatic stress is applied to a predetermined value at a constant stress rate of 0.75 MPa/min. The pore pressure is loaded to a predefined stress at a rate of 0.1MPa/min.

(3): The deviatoric stress $(\sigma_1 - \sigma_3)$ is increased by a constant strain rate of 0.02mm/min until the failure of the sample. During the whole process, the confining and pore pressures are kept constant.

3. Experimental results and discussion

3.1 Stress–strain curves

The stress-strain curves of dry fine-grained sandstone under confining pressure of 0, 3, 5, 10, 15, and 20 MPa are shown in Fig. 2. ε_1 and ε_3 are axial and lateral strain, respectively. $\sigma_1 - \sigma_3$ is deviatoric stress. According to the mechanical behaviors of the dry sandstone in previous investigations [4], the test curves can be divided into three typical stages before peak failure: the initial loading stage, linear elastic stage, and strain hardening stage. The stress-volumetric strain of dry fine-grained sandstone under various confining pressures is shown in Fig. 3. Due to closure of pre-existing microcracks, defects, and voids at the initial loading stages, volumetric strain increases linearly with the increase of deviatoric stress under different confining pressures at linear elastic stage. The maximum volumetric strain, which means that volumetric deformation of samples switches from

compaction to dilation, can be concluded as the result of pre-existing microcracks development and new microcracks initiation. Besides, the stress corresponding to the maximum volumetric strain is as initial yield strength. Then, the volumetric strain decreases nonlinearly with the increase of deviatoric stress due to the further stable and unstable of cracks.

The deviatoric stress-strain curves of saturated fine-grained sandstone under various confining and pore pressures are shown in Fig. 4. The black, red and blue lines are respectively axial, lateral and volumetric strain. p_w is pore pressure. The stress-strain curves of saturated fine-grained sandstone are divided into four stages: initial nonlinear stage, linear elastic stage, strain hardening stage and post-peak failure stage. The axial peak strain of saturated fine-grained sandstone are 9.25, 10.02, and 9.83‰ under the pore pressure of 6 MPa and confining pressures of 10, 15, and 20 MPa, approximately discrepancy 7.42, -0.63, and -4.33% of dry fine-grained sandstone under corresponding confining pressure. Whereas, the lateral peak strain of saturated fine-grained sandstone are -10.01, -7.10, and -5.48‰ approximately 150.16, 3.46, and 56.30% more than that of dry fine-grained sandstone under corresponding confining pressure. The results indicate that lateral deformation is more sensitive to confining pressure. The axial peak strain of saturated fine-grained sandstone are 9.20, 9.25, and 7.97‰ under confining pressure of 10 MPa and confining pressure pressures of 4, 6, and 8 MPa, approximately discrepancy 6.78, 7.42, and -7.43% of dry fine-grained sandstone under corresponding confining pressure. Nonetheless, the lateral peak strain of saturated fine-grained sandstone are -7.28, -10.01, and -5.46‰ approximately more than 82.04, 150.16, and 36.58% of dry fine-grained sandstone under corresponding confining pressure. The results indicate that lateral deformation is more sensitive to pore pressure. Because friction and cohesion between grain particles weakened by water accelerates lateral damage evolution.

3.2 Mechanical behaviors of fine-grained sandstone

The mechanical parameters of dry fine-grained sandstone under different confining pressure are listed in Table 1. The mechanical parameters of saturated fine-grained sandstone under different confining and pore pressures are listed in Table 2. The results indicate that mechanical behaviors of saturated fine-grained sandstone are close relation to confining and pore pressure.

In triaxial compression condition $(\sigma_2 = \sigma_3)$, the deviatoric pressure q equals to $\sigma_1 - \sigma_3$ and the mean stress p equals to $(\sigma_1 + 2\sigma_3)/3$. The initial yield strength envelope of dry fine-grained is fitted

by $q = 3.73(p + 2.0)^{0.9}$ with a correlation coefficient of 0.994, while the peak strength envelope is fitted by $q = 4.11(p + 2.0)^{0.9}$ with a correlation coefficient of 0.998. As to saturated fine-grained sandstone, extend the strength envelope of dry fine-grained sandstone to saturated porous media by using principle of effective stress. p' is the effective mean stress while q' is the effective deviatoric stress. b is Biot's coefficient. Therefore, a yield function of dry and saturated fine-grained sandstone in the plane ($p^{'}$, $q^{'}$) at initial yield stress and peak stress are plotted in Fig. 5. A fitting curve of initial yield stress envelope is $q^{'} = 3.73(p^{'} + 2.0)^{0.9}$ with a correlation coefficient of 0.996, while fitting function of peak strength envelope is $q^{'} = 4.11(p^{'} + 2.0)^{0.9}$ with a correlation coefficient of 0.997. b equals to 0.85 by repeated calculation.

3.3 Specific model for the sandstone

Based on experimental results, a new nonlinearly yield criterion is to describe the mechanical behaviors of dry and saturated fine-grained sandstone. Taking compressive stress as positive, the plastic yield function is written as

$$f_p = q^{'} + \frac{1}{k}\alpha_p h(\theta)\left(\frac{p^{'}+C_0}{p_0}\right)^n \quad (1)$$

with

$$p^{'} = \frac{\sigma_{kk}^{'}}{3},\ q^{'} = \sqrt{3J_2^{'}},\ J_2^{'} = \frac{1}{2}s_{ij}^{'}s_{ij}^{'},\ s_{ij}^{'} = \sigma_{ij}^{'} - \frac{\delta_{ij}}{3}\sigma_{kk}^{'},\ \sigma_{ij}^{'} = \sigma_{ij} - bp_w\delta_{ij} \quad (2)$$

where $\sigma_{kk}^{'}$ is effective volumetric stress, and δ_{ij} is the Kronecker Delta. Function $h(\theta)$ expresses the dependency of mechanical behaviors on the Lode angle θ. For simplicity, $h(\theta)$ is considered equal to 1. A fixed reference pressure p_0=1 MPa is used to adjust the units of the equation. C_0 is related to cohesion, determined by drawing the peak strength envelope in $p^{'} - q^{'}$ plane. The plastic hardening/softening function α_p is in terms of an increasing function of the generalized plastic shear strain γ_p and a decreasing function of the damage variable ω, which is written as

$$\alpha_p = -k(1 - \chi\omega)\left[\alpha_1 - (\alpha_1 - \alpha_0)exp\left(-\beta\gamma_p\right)\right] \quad (3)$$

$$d\gamma_{\mathrm{p}} = \int\sqrt{\frac{2}{3}de_{ij}^{p}de_{ij}^{p}},\ e_{ij}^{p} = \varepsilon_{ij}^{p} - \frac{1}{3}tr(\boldsymbol{\varepsilon}^{\mathrm{p}})\delta_{ij} \quad (4)$$

where α_1 and α_0 are material parameters. Parameter β determines the plastic hardening rate. χ is taken as a model parameter coupling damage evolution and plastic deformation.

Based on experimental results of saturated fine-grained sandstone, the plastic potential had better

consider the effect of pore pressure. Inspired by the work of [27], the plastic potential function is defined as

$$g = q'h(\theta) - \eta(1-\chi\omega)\left(1 + A\frac{p_w}{p_0}\right)(p' + C_0)ln\left(\frac{p'+C_0}{I_0}\right) = 0 \tag{5}$$

where I_0 defines the intersection of the potential surface with the p' axis. Using this potential, the stress space is divided into plastic compression and dilation zones. The boundary between these two zones is defined by the condition of $\frac{\partial g}{\partial p'} = 0$. In this model, this boundary is determined by the following linear function:

$$f_b = q'h(\theta) + \eta(1-\chi\omega)\left(1 + A\frac{p_w}{p_0}\right)(p' + C_0) \tag{6}$$

Similar to the plastic theory, a scalar damage criterion with an associated flow rule is used to describe damage evolution. According to the research of statistical damage theory [28], an exponential function on the Y_d can be used to describe the damage evolution.

$$f_d = \omega_c\{1 - exp(-B_\omega(Y_d - Y_d^0))\} - \omega \tag{7}$$

where ω_c is the maximum damage, parameter B_ω controls the kinetics of the damage evolution, and Y_d^0 is the damage thermodynamic force threshold. The thermodynamic force with the damage variable is given by:

$$Y_d = -\frac{1}{2}(\boldsymbol{\varepsilon} - \boldsymbol{\varepsilon}^p):\frac{\partial \mathbf{C}(\omega)}{\partial \omega}:(\boldsymbol{\varepsilon} - \boldsymbol{\varepsilon}^p) + k\chi\left[\alpha_1\gamma_p + \frac{(\alpha_1-\alpha_0)}{\beta}exp(-\beta\gamma_p)\right] \tag{8}$$

3.4 Coupled elastoplastic damage implementation algorithm

The returning mapping method [29] is an efficient to implement elastoplastic model. In order to draw stress sate back to the plastic surface, the elastoplastic damage coupled correction algorithm is composed of elastic prediction and plastic and damage correction. The efficiency of the numerical method has been demonstrated in [5]. When plastic and damage constituency condition are in coupled system in effective stress space, equation system at (k+1)th loading step can be described as first-order Taylor expansion

$$\begin{cases} f_{p,m+1}^{k+1} = f_{p,m}^{k+1} + \frac{f_{p,m}^{k+1}}{\partial \boldsymbol{\sigma}'}:\Delta\boldsymbol{\sigma}' + \frac{f_{p,m}^{k+1}}{\gamma_p}\Delta\gamma_p + \frac{f_{p,m}^{k+1}}{\omega}\Delta\omega \approx 0 \\ f_{d,m+1}^{k+1} = f_{d,m}^{k+1} + \frac{f_{d,m}^{k+1}}{Y_d}\Delta Y_d + \frac{f_{d,m}^{k+1}}{\omega}\Delta\omega \approx 0 \end{cases} \tag{9}$$

where the subscript m is the index of inner iteration in recycling of (k+1)th loading step. .

$$\Delta\boldsymbol{\sigma}' = -\mathbf{C}(\omega):\Delta\boldsymbol{\varepsilon}^p + \frac{\partial\mathbf{C}(\omega)}{\partial\omega}:(\boldsymbol{\varepsilon}-\boldsymbol{\varepsilon}^p)\Delta\omega - b\boldsymbol{\delta}\Delta p_w \quad (10\text{-a})$$

$$\Delta Y_d = -\frac{\partial Y_d}{\partial\boldsymbol{\varepsilon}^e}:\Delta\boldsymbol{\varepsilon}^p + \frac{\partial Y_d}{\partial\gamma_p}\Delta\gamma_p \quad (10\text{-b})$$

$$\Delta\gamma_p = \Delta\lambda_p\frac{\partial g}{\partial q} \quad (10\text{-c})$$

$$\Delta\omega = \Delta\lambda_d\frac{\partial f_{d,m}^{k+1}}{\partial Y_d} \quad (10\text{-d})$$

The plastic multiplier $\Delta\lambda_p$ and damage multiplier $\Delta\lambda_d$ are determined simultaneously by solving a set of linear equations of the plastic and damage consistency conditions.

$$\begin{pmatrix}A_{11} & A_{12}\\ A_{21} & A_{22}\end{pmatrix}\begin{pmatrix}\Delta\lambda_d\\ \Delta\lambda_p\end{pmatrix} = \begin{pmatrix}B_1\\ B_2\end{pmatrix} \quad (11)$$

According to Eq. (9), the plastic multiplier $\Delta\lambda_p$ and damage multiplier $\Delta\lambda_d$ are obtained as follows

$$\Delta\lambda_d = \frac{B_1A_{22}-B_2A_{12}}{A_{11}A_{22}-A_{21}A_{12}} \quad (12)$$

$$\Delta\lambda_p = \frac{B_2A_{11}-B_1A_{21}}{A_{11}A_{22}-A_{21}A_{12}} \quad (13)$$

In which A_{11}, A_{12}, A_{21}, A_{22}, B_1, and B_2 are defined as follows:

$$A_{11} = \frac{\partial f_{p,m}^{k+1}}{\partial\boldsymbol{\sigma}'}:\mathbf{C}_0:(\boldsymbol{\varepsilon}-\boldsymbol{\varepsilon}^p) - \frac{\partial f_{p,m}^{k+1}}{\partial\omega}\frac{\partial f_{d,m}^{k+1}}{\partial Y_d},\ A_{12} = \frac{\partial f_{p,m}^{k+1}}{\partial\boldsymbol{\sigma}'}:\mathbf{C}(\omega):\frac{\partial g}{\partial\boldsymbol{\sigma}'} - \frac{\partial f_{p,m}^{k+1}}{\partial\gamma_p}\frac{\partial g}{\partial q}$$

$$A_{21} = -\frac{\partial f_{d,m}^{k+1}}{\partial\omega}\frac{\partial f_{d,m}^{k+1}}{\partial Y_d},\ \mathrm{A}_{22} = -\frac{\partial f_{d,m}^{k+1}}{\partial Y_d}\left[\mathbf{C}_0:(\boldsymbol{\varepsilon}-\boldsymbol{\varepsilon}^p):\frac{\partial g}{\partial\boldsymbol{\sigma}'} + \frac{\partial Y_d}{\partial\gamma_p}\frac{\partial g}{\partial q'}\right]$$

$$B_1 = f_{p,m}^{k+1} + \mathrm{b}\dot{p}_w\frac{\partial f_{p,m}^{k+1}}{\partial\boldsymbol{\sigma}'}:\boldsymbol{\delta},\ B_2 = f_{d,m}^{k+1}.$$

4. Numerical implementation

Because the triaxial compression test is conducted using the axial strain-controlled, the algorithmic implementation is described by a step-by-step procedure within the strain-driven procedure. A flowchart of decoupling correction algorithm is shown in Table 3.

5. Model validation

All of model parameters can be obtained from the triaxial compression test of fine-grained sandstone. The elastic modulus E and the Poisson' ratio ν are determined by the linear part of the stress–strain curves, as shown in Table 1. Parameters α_1 and C_0 can be determined by the slope and the intercept of the strength envelope with the p axis, respectively. Parameters α_0 and η can be

deduced by the initial yield surface. Parameter β is obtained by fitting the plastic hardening segment of the stress–strain curves. The damage thermodynamic force threshold Y_d^0 is determined by the transition point at which the volumetric deformation switches from compaction to dilation. The maximum damage value ω_c can be obtained by triaxial cyclic loading tests. The damage parameters k, B_ω, and χ are difficult to be calibrated directly from the test data. Therefore, they are estimated by trial-and-error to obtain a good simulation result.

Based on the triaxial compression experimental data, the model parameters for dry fine-grained sandstone are determined and the results are shown in Table 4. A comparison between the numerical simulation and laboratory test results of dry fine-grained sandstone under different confining pressures is presented in Fig. 6. Due to the initial compression stage not taken into consideration in the proposed model, the experimental data have been processed by ignoring the initial nonlinear deformation. The triaxial compression test of saturated fine-grained sandstone under various confining and pore pressures can be described by the same constitutive model. The added parameters of the model for saturated sandstone are as follows: $A = 0.077$ and $b = 0.85$. A comparison between the numerical simulation and laboratory test results of saturated fine-grained sandstone under different confining and pore pressures is presented in Fig. 7. The comparison results indicate that there is a good agreement between the modeling results and the experimental results. In fact, microcracks propagation through grain interfaces of fine-grained sandstone are dependent on stress state. Such nonproportional loading paths can lead to a strong stress-induced anisotropy. Namely, the discrepancy between test results and numerical results is caused by anisotropic damage evolution.

6. Conclusions

In order to investigate the hydromechanical properties of the fine-grained sandstone, a series of triaxial compression tests of dry and saturated fine-grained sandstone are carried out. Test results show that mechanical parameters are strong correlation with confining pressure and pore pressure. The stress-strain curves of saturated fine-grained sandstone are divided into three stages pre-peak and post-peak region. The comparing results indicate that effect of confining pressure and pore pressure on axial strain is not obvious. However, the lateral strain is more sensitive on confining and pore pressures. Based on the experimental results, a nonlinear model considering the influences of pore pressure, irreversible deformation and damage evolution is proposed. The validity of the proposed coupled

model accounting simultaneously for the coupling of plastic deformation, damage evolution and pore pressure is confirmed by experimental data and the numerical simulation results. The model captures the main features of strain-hardening, strain-softening, shear dilation, and hydro-mechanical behaviors of the fine-grained sandstone. Further investigations on partially saturated material, anisotropic damage evolution behaviors of fine-grained sandstone will need to be considered in future work.

Acknowledgments

Financial supports provided by the National Key R&D Program of China (2017YFC1501100), Postgraduate Research & Practice Innovation Program of Jiangsu Province (Grant No. KYCX17_0471, 2017B700X14), the Natural Science Foundation of China (Grant No. 51479049) are gratefully acknowledged.

References

1. Chen L, Wang CP, Liu JF, et al. Damage and plastic deformation modeling of Beishan granite under compressive stress conditions. Rock Mech Rock Eng. 2015;48(4): 1623-1633.

2. Parisio F, Samat S, Laloui L. Constitutive analysis of shale: a coupled damage plasticity approach. Int J Solids Struct. 2015;75-76: 88-98.

3. Zhang JC, Xu WY, Wang HL, Wang RB, Meng QX, Du SW. A coupled elastoplastic damage model for brittle rocks and its application in modelling underground excavation. Int J Rock Mech Min Sci. 2016;84: 130-141.

4. Wang S, Xu W, Jia C, Wang W. Mechanical behavior of fine-grained sandstone in triaxial compression and elastoplastic modeling by return mapping algorithms. Bull Eng Geol Environment. 2017: 1-11.

5. Wang S, Xu W, Wang W, Jia C. Experimental and numerical investigations on the mechanical behavior of fine-grained sandstone. Int J Geomech. 2018;18(2): 04017150.

6. Wang HL, Xu WY, Jia CJ, Cai M, Meng QX. Experimental research on permeability evolution with microcrack development in sandstone under different fluid pressures. J Geotech Geoenviron Eng. 2016;142(6): 04016014.

7. Wang HL, Xu WY, Shao JF. Experimental researches on hydro-mechanical properties of altered rock under confining pressures. Rock Mech Rock Eng. 2014;47(2): 485-493.

8. Liu Z, Shao J. Strength behavior, creep failure and permeability change of a tight marble under triaxial compression. Rock Mech Rock Eng. 2017;50(3): 1-13.

9. Hatzor YH, Palchik V. The influence of grain size and porosity on crack initiation stress and critical flaw length in dolomites. Int J Rock Mech Min Sci. 1997;34(5): 805-816.

10. Wasantha PLP, Ranjith PG, Zhao J, Shao SS, Permata G. Strain rate effect on the mechanical behaviour of sandstones with different grain sizes. Rock Mech Rock Eng.

2015;48(5): 1883-1895.

11. Fredrich JT, Evans B, Wong TF. Effect of grain size on brittle and semibrittle strength: Implications for micromechanical modelling of failure in compression. J Geophys Res Solid Earth. 1990;95(B7): 10907–10920.

12. Zhu QZ, Shao JF. A refined micromechanical damage–friction model with strength prediction for rock-like materials under compression. Int J Solids Struct. 2015;s 60–61: 75-83.

13. Pens, Eacute V, Kondo D, Dormieux L. Micromechanical analysis of anisotropic damage in brittle materials. J Eng Mech. 2002;128(8): 889-897.

14. Qi M, Shao JF, Giraud A, Zhu QZ, Colliat JB. Damage and plastic friction in initially anisotropic quasi brittle materials. Int J Plast. 2016;82: 260-282.

15. Chen Y, Wang Y, Zhang QY. Coupled seepage-elastoplastic-damage analysis of saturated porous media and its application to water conveyance tunnel. Tunnell Undergr Space Tech. 2014;44(3): 80-87.

16. Bui TA, Wong H, Deleruyelle F. Thermodynamically consistent modelling of viscoplasticity and damage coupling in saturated rocks. Géotechnique Letts. 2016;6(1): 1-5.

17. Biot MA. General theory of three-dimensional consolidation. J Appl Phys. 1941;12(2): 155-164.

18. Bishop AW, Blight GE. Some aspects of effective stress in saturated and partly saturated soils. Géotechnique. 1963;13(3): 177-197.

19. Dufour N, Wong H, Arson C, Deleruyelle F, Pereira JM. A thermodynamically consistent framework for saturated viscoplastic rock-materials subject to damage. Mech Res Comm. 2012;45: 15-21.

20. Biot MA. Mechanics of Deformation and Acoustic Propagation in Porous Media. J Appl Phys. 1962;33(4): 1482-1498.

21. Hamiel Y, Lyakhovsky V, Agnon A. Coupled evolution of damage and porosity in poroelastic media: theory and applications to deformation of porous rocks. Geophys J Roy Astron Soc. 2010;156(3): 701-713.

22. Shao JF, Jia Y, Kondo D, Chiarelli AS. A coupled elastoplastic damage model for semi-brittle materials and extension to unsaturated conditions. Mech Mater. 2006;38(3): 218-232.

23. Coussy O, Pereira JM, Vaunat J. Revisiting the thermodynamics of hardening plasticity for unsaturated soils. Comput Geotech. 2010;37(1–2): 207-215.

24. Bui TA, Wong H, Deleruyelle F, Xie LZ, Tran DT. A thermodynamically consistent model accounting for viscoplastic creep and anisotropic damage in unsaturated rocks. Int J Solids Struct. 2017.

25. Xie SY, Shao JF. An experimental study and constitutive modeling of saturated porous rocks. Rock Mech Rock Eng. 2015;48(1): 223-234.

26. Hamiel Y, Lyakhovsky V, Agnon A. Coupled evolution of damage and porosity in poroelastic media: theory and applications to deformation of porous rocks. Geophys J Roy Astron Soc. 2004;156(3): 701-713.

27. Pietruszczak S, Jiang J, Mirza FA. An elastoplastic constitutive model for concrete. Int J Solids Struct. 1988;24(7): 705-722.

28. Parisio F, Samat S, Laloui L. Constitutive analysis of shale: a coupled damage plasticity approach. Int J Solids Struct. 2015;s 75–76: 88-98.

29. Simo JC, Ortiz M. A unified approach to finite deformation elastoplastic analysis based on the use of hyperelastic constitutive equations. Comp Meth Appl Mech Eng. 1985;49(2): 221-245.

Table Headings

Table 1. Mechanical parameters obtained from triaxial compression tests of dry fine-grained sandstone.

Table 2. Mechanical parameters obtained from triaxial compression tests of saturated fine-grained sandstone.

Table 3. The decoupled algorithm of numerical implementation of the proposed model.

Table 4. Mechanical parameters used for modeling the triaxial compression tests of the dry fine-grained sandstone.

Figure Captions

Fig. 1. Typical fine-grained sandstone samples: (*a*) dry; (*b*) saturated.

Fig. 2. Deviatoric stress–strain curves obtained from triaxial compression of dry fine-grained sandstone under different confining pressures.

Fig. 3. Deviatoric stress–volumetric strain curves obtained from triaxial compression of dry fine-grained sandstone under different confining pressures.

Fig. 4. Deviatoric stress–strain curves obtained from triaxial compression of saturated fine-grained sandstone under different confining pressures and water pressures. (*a*) σ_3= 10 MPa, p_w= 4 MPa; (*b*) σ_3= 10 MPa, p_w= 6 MPa ; (*c*) σ_3= 10 MPa, p_w= 8 MPa; (*d*) σ_3= 15 MPa, p_w= 6 MPa ; (*e*) σ_3= 20 MPa, p_w= 6 MPa.

Fig. 5. Relations between the effective deviatoric stress q' and the effective mean stress p' at initial yield and peak stress (" $'$ " denotes as "effective" with pore pressure).

Fig. 6 Simulation of triaxial compression tests of dry fine-grained sandstone under various confining pressures: *a*. σ_3=20 MPa; *b*. σ_3=15 MPa; *c*. σ_3=10 MPa; *d*. σ_3=5 MPa; *e*. σ_3=3 MPa.

Fig. 7. Simulation of triaxial compression tests under various initial confining and water pressures: *a*. σ_3=20 Mpa, p_w=6 MPa; *b*. σ_3=15 Mpa, p_w=6 MPa; *c*. σ_3=10 Mpa, p_w=4 MPa; *d*. σ_3=10 Mpa, p_w=6 MPa; *e*. σ_3=10 Mpa, p_w=8 MPa.

(*a*) (*b*)

Fig. 1 Typical fine-grained sandstone samples: (*a*) dry; (*b*) saturated.

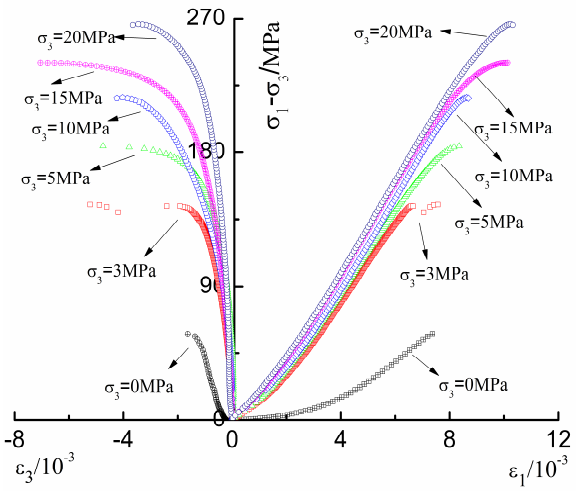

Fig. 2. Deviatoric stress–strain curves obtained from triaxial compression of dry fine-grained sandstone under different confining pressures.

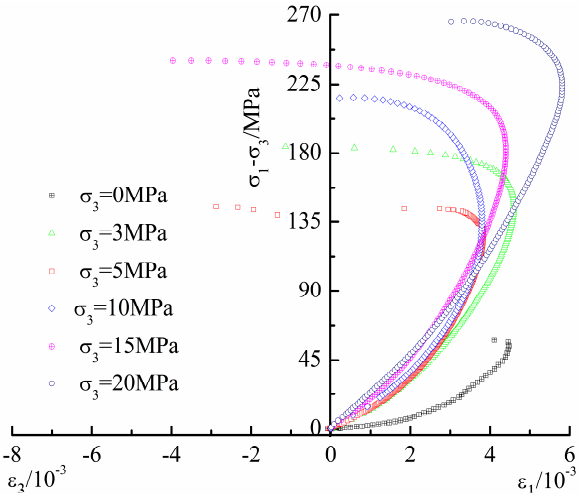

Fig. 3. Deviatoric stress–volumetric strain curves obtained from triaxial compression of dry fine-grained sandstone under different confining pressures.

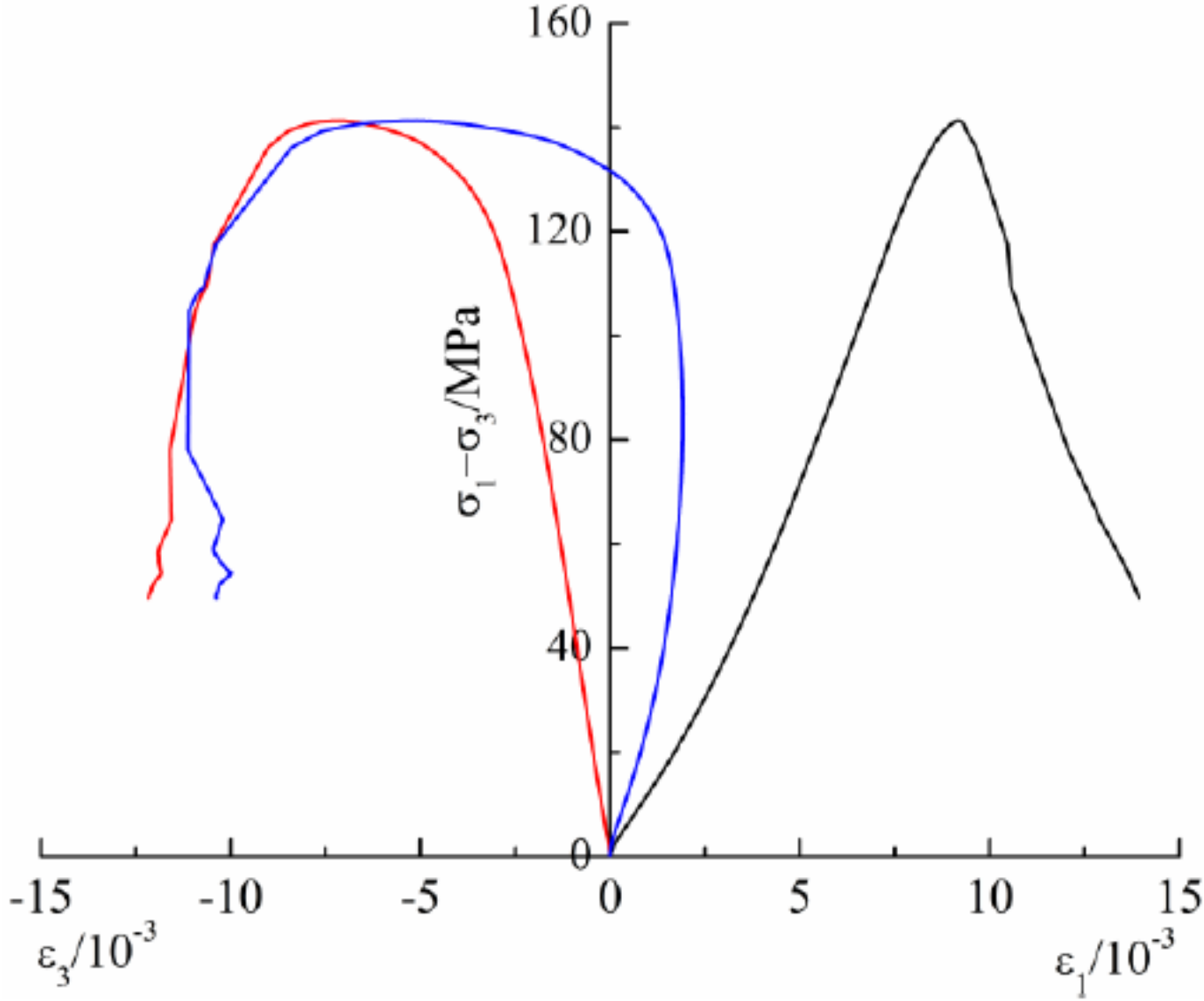

(*a*) σ_3= 10 MPa, p_w= 4 MPa

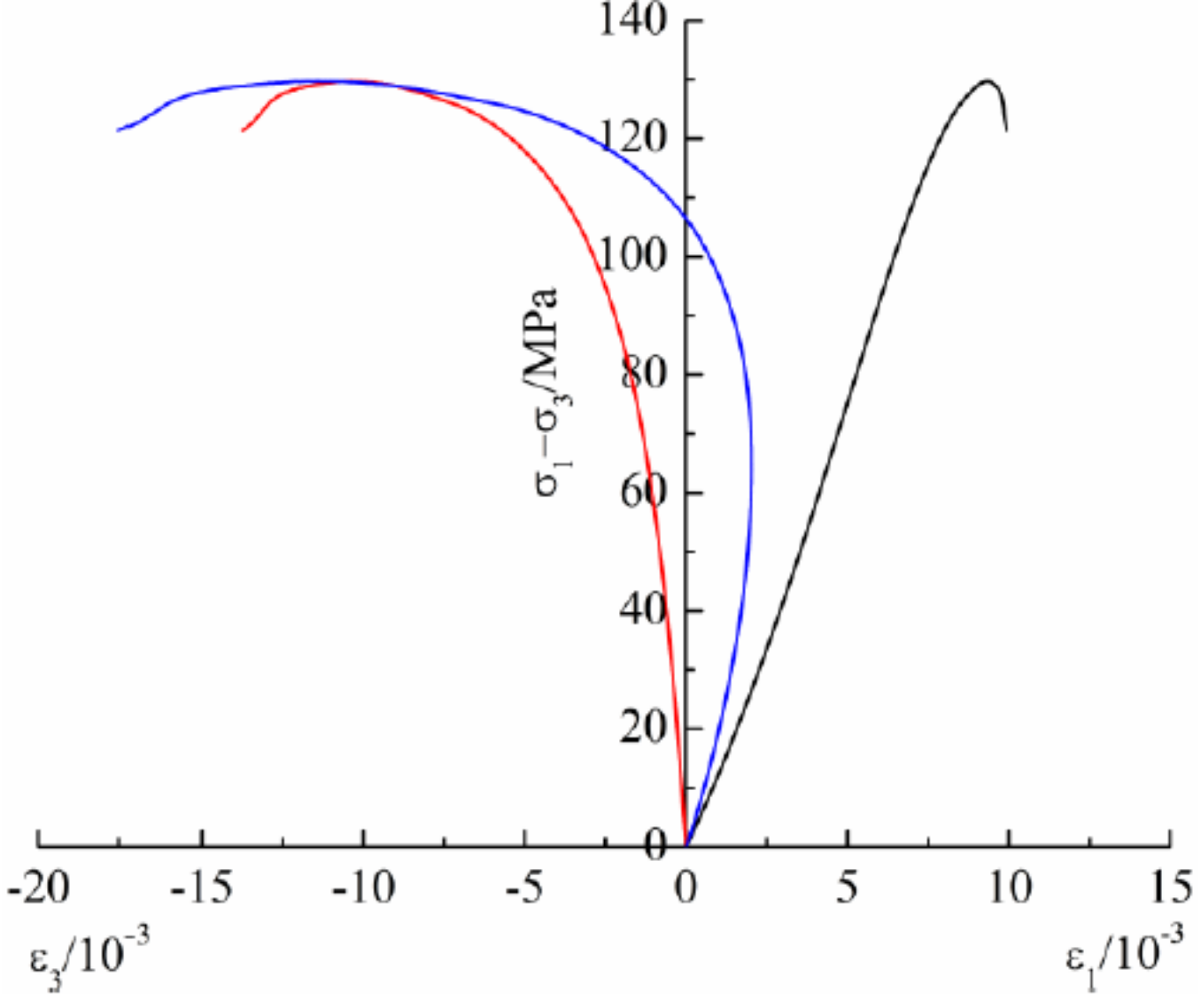

(*b*) σ_3= 10 MPa, p_w= 6 MPa

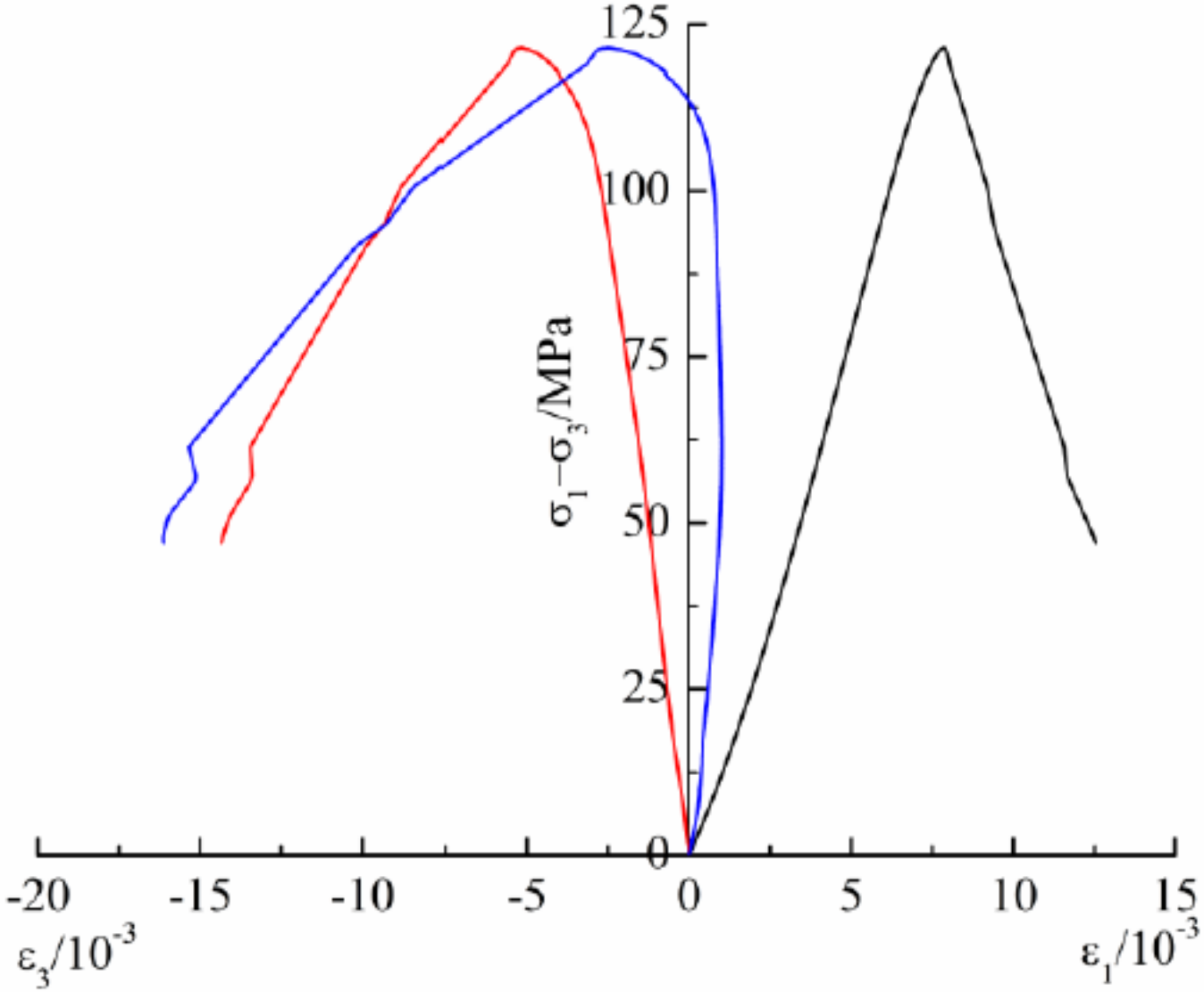

(*c*) σ_3= 10 MPa, p_w= 8 MPa

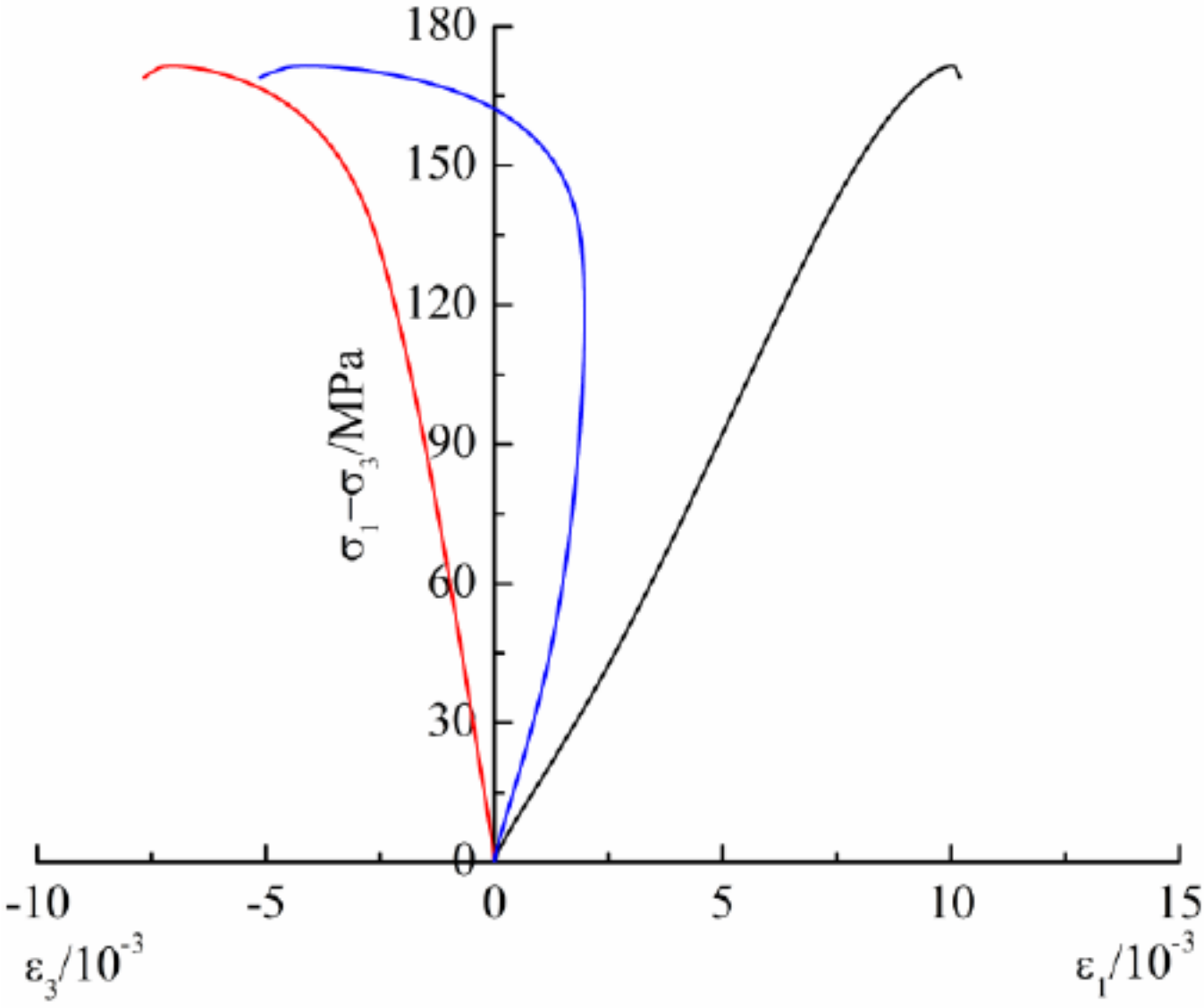

(*d*) σ_3= 15 MPa, p_w= 6 MPa

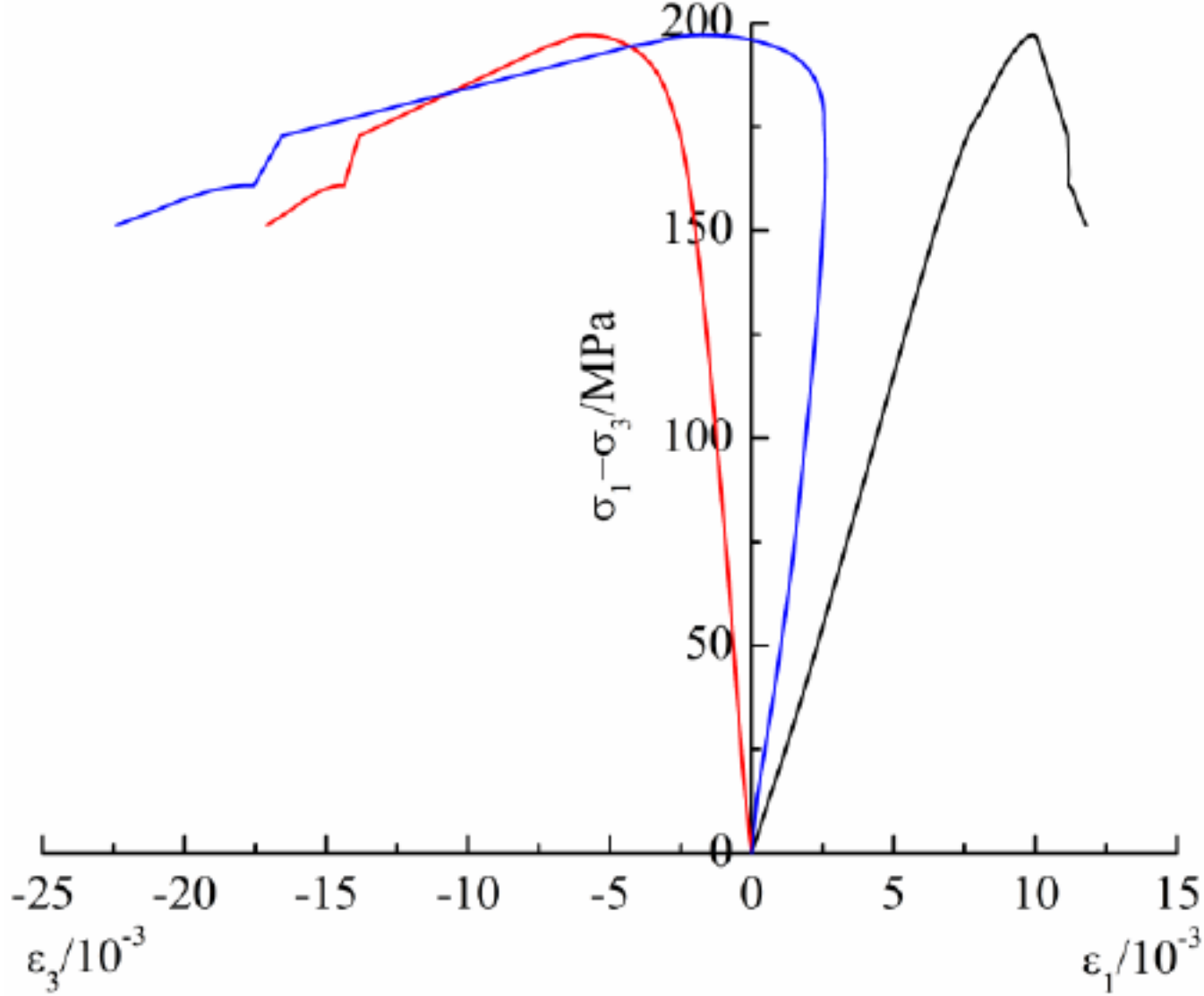

(*e*) σ_3= 20 MPa, p_w= 6 MPa

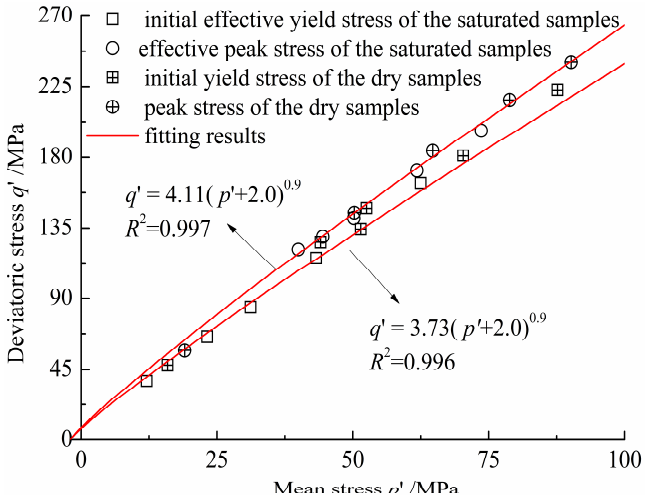

Fig. 5. Relations between the effective deviatoric stress q' and the effective mean stress p' at initial yield and peak stress (" $'$ " denotes as "effective" with pore pressure).

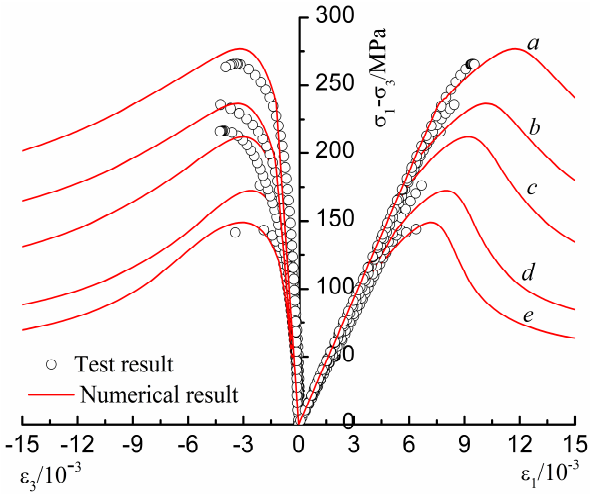

Fig. 6 Simulation of triaxial compression tests of dry fine-grained sandstone under various confining pressures: *a*. σ_3=20 MPa; *b*. σ_3=15 MPa; *c*. σ_3=10 MPa; *d*. σ_3=5 MPa; *e*. σ_3=3 MPa.

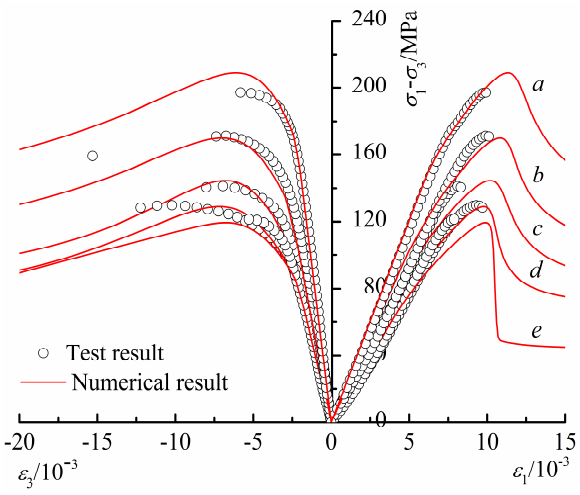

Fig. 7. Simulation of triaxial compression tests under various initial confining and water pressures: *a*. σ_3=20 Mpa, p_w=6 MPa; *b*. σ_3=15 Mpa, p_w=6 MPa; *c*. σ_3=10 Mpa, p_w=4 MPa; *d*. σ_3=10 Mpa, p_w=6 MPa; *e*. σ_3=10 Mpa, p_w=8 MPa.

Table 1. Mechanical parameters obtained from triaxial compression tests of dry fine-grained sandstone

Confining pressure σ_3 (MPa)	Elastic modulus E (GPa)	Poisson's ratio ν	Initial yield strength (MPa)	Peak strength σ_p (MPa)
0	13.80	0.19	47.73	57.18
3	27.18	0.20	126.22	144.81
5	27.87	0.16	147.58	184.07
10	30.05	0.19	134.40	216.57
15	31.06	0.20	180.89	240.50
20	31.12	0.16	222.95	266.08

Table 2. Mechanical parameters obtained from triaxial compression tests of saturated fine-grained sandstone

Confining pressure σ_3 (MPa)	Water pressure p_w (MPa)	Elastic modulus E (GPa)	Poisson's Ratio ν	Initial yield stress σ_y (MPa)	Peak strength σ_p (MPa)
10	4	18.67	0.47	84.39	141.32
	6	17.00	0.48	65.77	129.61
	8	14.06	0.48	37.83	121.5
15	6	20.56	0.42	115.99	171.52
20		24.14	0.32	163.64	197.11

Table 3. The coupled algorithm of numerical implementation of the proposed model.

Input: $\boldsymbol{\sigma}^{',k}$, $\boldsymbol{\varepsilon}^{k}$, $\boldsymbol{\varepsilon}_{p}^{k}$, γ_{p}^{k}, ω^{k}

for $k = 0,\ldots,$sum

Elastic prediction

$\boldsymbol{\varepsilon}^{k+1} = \boldsymbol{\varepsilon}^{k} + d\boldsymbol{\varepsilon}^{k+1}$

$\boldsymbol{\sigma}^{',k+1} = \boldsymbol{\sigma}^{',k} + \mathbf{C}(\omega)\colon d\boldsymbol{\varepsilon}^{k+1}$

$\gamma_{p}^{k+1} = \gamma_{p}^{k}$

$\omega^{k+1} = \omega^{k}$

if $f_{p}\left(\boldsymbol{\sigma}^{',k+1}, \gamma_{p}^{k+1}, \omega^{k+1}\right) \geq 0$ and $f_{d}\left(Y_{d}^{k+1}, \omega^{k+1}\right) \geq 0$

Coupled plastic-damage corrections

while $\left(f_{p}\left(\boldsymbol{\sigma}^{',k+1}, \gamma_{p}^{k+1}, \omega^{k+1}\right) < f_{tol} \;\; or \; f_{d}\left(Y_{d}^{k+1}, \omega^{k+1}\right) < f_{tol}\right)$

The plastic multipliers $\Delta\lambda_{p}^{k+1}$ and damage multipliers $\Delta\lambda_{d}^{k+1}$ are determined by the equations (12) and (13). Then, the plastic stress and tensor, damage and other internal variables are updated as follows

$$\boldsymbol{\varepsilon}_{k+1}^{p} = \boldsymbol{\varepsilon}_{k+1}^{p} + \Delta\lambda_{p}^{k+1}\frac{\partial g}{\partial \boldsymbol{\sigma}'}$$

$$\omega^{k+1} = \omega^{k+1} + \Delta\lambda_{d}^{k+1}\frac{\partial f_{d}^{k+1}}{\partial Y_{d}}$$

$$\gamma_{p}^{k+1} = \gamma_{p}^{k+1} + \Delta\lambda_{p}\left[\frac{\partial \gamma_{p}}{\partial \boldsymbol{\varepsilon}_{p}}\right]^{T}\colon\frac{\partial g}{\partial \boldsymbol{\sigma}'}$$

$$\Delta\boldsymbol{\sigma}_{pd}^{'} = -\Delta\lambda_{p}^{k+1}\mathbf{C}(\omega)\colon\frac{\partial g}{\partial \boldsymbol{\sigma}'} - \Delta\lambda_{d}^{k+1}\mathbf{C}_{0}\colon\boldsymbol{\varepsilon}^{e}$$

$$\boldsymbol{\varepsilon}^{e,k+1} = \boldsymbol{\varepsilon}^{e,k+1} + \mathbf{D}(\omega)\colon\delta\boldsymbol{\sigma}_{pd}^{'}$$

$$\boldsymbol{\sigma}^{',k+1} = \boldsymbol{\sigma}^{',k} + \Delta\boldsymbol{\sigma}_{pd}^{'}$$

$$Y^{k+1} = Y^{k+1} + \Delta\lambda_{p}\left[\frac{\partial Y^{p}}{\partial \gamma_{p}}\left(\frac{\partial \gamma_{p}}{\partial \boldsymbol{\varepsilon}_{p}}\right)^{T}\colon\frac{\partial g}{\partial \boldsymbol{\sigma}'} + (\boldsymbol{\varepsilon}^{e})^{T}\colon\mathbf{C}_{0}\colon\frac{\partial g}{\partial \boldsymbol{\sigma}'}\right]$$

Output: $\boldsymbol{\sigma}^{',k+1}$, $\boldsymbol{\varepsilon}^{k+1}$, γ_{p}^{k+1}, ω^{k+1}

Table 4 Mechanical parameters used for modeling the triaxial compression tests of the dry fine-grained sandstone.

Plastic parameters						Damage parameters			
C_0 (MPa)	α_1	α_0	η	β	χ	Y_d^0	k	B_ω	ω_c
2.0	4.566	3.730	-2.552	1500	1.0	0.3017 0.4097 0.3314 0.5857 0.9092	40.0	1.0	0.3